Research Article

Nano Research
2020, 13(9): 2534–2540

ISSN 1998-0124 CN 11-5974/O4
https://doi.org/10.1007/s12274-020-2892-8

Quasiparticle interference and impurity resonances on WTe_2

Hyeokshin Kwon[1,§], Taehwan Jeong[2,§], Samudrala Appalakondaiah[2,3,§], Youngtek Oh[1], Insu Jeon[1], Hongki Min[4], Seongjun Park[1] (✉), Young Jae Song[2,3,5,6] (✉), Euyheon Hwang[2,3] (✉), and Sungwoo Hwang[1]

[1] *Samsung Advanced Institute of Technology, Samsung Electronics Co., Suwon 16678, Republic of Korea*
[2] *SKKU Advanced Institute of Nano Technology (SAINT), Sungkyunkwan University, Suwon 16419, Republic of Korea*
[3] *Department of Nano Engineering, Sungkyunkwan University, Suwon 16419, Republic of Korea*
[4] *Department of Physics and Astronomy, Seoul National University, Seoul 08826, Republic of Korea*
[5] *Department of Physics, Sungkyunkwan University, Suwon 16419, Republic of Korea*
[6] *Center for Integrated Nanostructure Physics (CINAP), Institute for Basic Science (IBS), Sungkyunkwan University, Suwon 16419, Republic of Korea*
[§] *Hyeokshin Kwon, Taehwan Jeong, and Samudrala Appalakondaiah contributed equally to this work.*

Received: 26 September 2019 / **Revised:** 14 May 2020 / **Accepted:** 21 May 2020

ABSTRACT

Using scanning tunneling microscopy/spectroscopy (STM/STS), we examine quasiparticle scattering and interference properties at the surface of WTe_2. WTe_2, layered transition metal dichalcogenide, is predicted to be a type-II Weyl semimetal. The Weyl fermion states in WTe_2 emerge as topologically protected touching points of electron and hole pockets, and Fermi arcs connecting them can be visible in the spectral function on the surface. To probe the properties of surface states, we have conducted low-temperature STM/STS (at 2.7 K) on the surfaces of WTe_2 single crystals. We visualize the surface states of WTe_2 with atomic scale resolution. Clear surface states emerging from the bulk electron pocket have been identified and their connection with the bulk electronic states shows good agreement with calculations. We show the interesting double resonance peaks in the local density of states appearing at localized impurities. The low-energy resonant peak occurs near the Weyl point above the Fermi energy and it may be mixed with the surface state of Weyl points, which makes it difficult to observe the topological nature of the Weyl semimetal WTe_2.

KEYWORDS

WTe_2, Weyl semimetal, quasi-particle interference, scanning tunneling microscopy/spectroscopy

1 Introduction

Novel topological states of matter have attracted much attention in the past decades. Especially, much recent interest in condensed matter physics has focused on bulk chiral materials with a gapless band structure including three-dimensional (3D) Weyl and Dirac semimetals [1–13], in which the elementary low-energy noninteracting electronic energy dispersion is linear and can be written in terms of Weyl and massless Dirac Hamiltonians, respectively. In 3D Weyl semimetals, due to the topologically protected bulk quasiparticles the topological protected surface states exist. Topological Weyl semimetals (WSMs) are new states of quantum matter and they have been known to exist theoretically. Recently they have been found experimentally in a crystal lattice as low-energy quasiparticle excitations [14–18]. A nonmagnetic semimetal in the TaAs family with time-reversal symmetry and broken space-inversion symmetry was theoretically predicted to be a WSM and subsequent experimental verification has motivated intensive studies on topological semimetals [19–23]. In the Weyl fermion band structure, topologically protected Fermi arcs were predicted to exist on its surface connecting projections of two Weyl points with opposite chirality in the crystal lattice, and these have been confirmed to reside on the surface of TaAs in angle-resolved photoemission spectroscopy (ARPES) [19–21] and scanning tunneling microscopy/spectroscopy (STM/STS) [22, 23] experiments. In addition to standard type-I WSMs which have Weyl points with a point-like Fermi surface, type-II WSMs were recently proposed [24]. In type-II WSM the Weyl points emerge at the contact points of the electron and hole pockets. WTe_2 is one of the first predicted type-II WSM. WTe_2 with its noncentrosymmetric orthorhombic Td phase is a layered transition metal dichalcogenide, and the exotic electronic properties such as the nonsaturating magnetoresistance [25] and pressure-induced superconductivity [26, 27] have been experimentally reported. The existence of surface Fermi arcs is one of the interesting properties of topological WSMs. Thus, to understand the electronic properties of the topological surface states emerging out of the bulk electron-hole pockets the existence of surface states are needed for topological WSMs. Recent ARPES experiments on the type-II WSM WTe_2 indicate the existence of surface states, but these states do not clearly manifest a topological nature of type-II Weyl points in the bulk [28–32]. Thus, other experiments are required to probe the topological nature of the type-II WSM WTe_2.

In this work, we investigate detailed quasiparticle interference (QPI) and perform a scattering analysis on the surface of the type-II WSM WTe_2 to examine the surface properties of WTe_2.

Address correspondence to Seongjun Park, s3.park@samsung.com; Young Jae Song, yjsong@skku.edu; Euyheon Hwang, euyheon@skku.edu

Low-temperature STM/STS provide a direct way to study the surface states at the atomic scale through probing the local density of states (LDOS) in the vicinity of defects on the surface [33]. The Fourier-transformed (FT) STS mapping, therefore, has been usefully used to investigate the surface states of topological semimetals [22, 23, 34, 35], as a STM technique can provide a tunneling spectroscopic measurements for both the occupied and unoccupied states with an excellent spatial resolution as a complimentary tool of ARPES. The interference between the two partial waves caused by defects on the surface gives rise to a spatial modulation of the amplitude of the total wave, and the spatial modulation resulting from the scattering interference provides useful information on the topological nature of the WSMs. The FT of the spatial modulation of the LDOS amplitude represents a direct image of the scattering channels [36]. We also provide calculated results to demonstrate that quasiparticle scattering interference can indeed produce patterns similar to those observed by FT-STS. We perform a T-matrix calculation for the scattering resulting from a nonmagnetic single impurity potential by using the electronic properties from first-principles calculations, which establish clear QPI features of the surface states.

The scattering on the constant-energy surface strongly depends on both momentum and spin orientation. The scattering on the surface has been studied by investigating the energy-dependent QPI data in the FT-STS mapping in the momentum space as well as by analyzing the standing waves of energy-dependent differential conductance images at the atomic scale. We find that the experimentally-measured arc-like surface state exhibits good agreements with first-principle band structure calculations. However, we find that it is the part of topologically-trivial states, and the existence of the topologically protected Fermi arc in surface states of WTe_2 is still missing. The very interesting spectroscopic double resonances on the defect sites were observed, which are related to the broken inversion symmetry of the electronic structure from the Te vacancies. The low-energy resonant peak occurs near the Weyl point above the Fermi energy and it may be mixed with the surface state of Weyl points, which makes it difficult to observe the topological nature of the Weyl semimetal WTe_2 because the resonant peaks enhance the scattering of quasiparticles. The resonant peaks may give rise to unusual transport properties in WTe_2.

2 Experimental

2.1 Measurements

The STM/STS experiments were performed using a cryogenic STM that operates at 2.7 K in an ultrahigh vacuum. Single crystals of WTe_2 were cleaved *in situ* and moved to the STM head immediately. All measurements have been performed using chemically etched W tips treated by electron-beam heating and field emission. The dI/dV values were measured using a set-point current of I_t = 0.5–1.0 nA, a lock-in modulation voltage of V_{mod} = 2–5 mV, and a modulation frequency of f_{mod} = 997 Hz. The number of grid points for dI/dV maps is 500 × 500. The QPI patterns from dI/dV maps at various energies were FT to reveal the electronic structure in a momentum space. To increase the signal-to-noise ratio, the FT amplitude maps have been mirror-symmetrized.

2.2 Computational details

The theoretical calculations were performed with Vienna *ab initio* simulation package (VASP) [37, 38] based on density functional theory (DFT). The exchange-correlational potential of Ceperley and Alder as parameterized by Perdew and Zunger (CAPZ) in local density approximation (LDA), is used [41, 42]. The interaction between core and valance electrons was represented by projector augmented wave potentials [43, 44]. The wave functions were expanded in plane wave approach with a kinetic cutoff of 450 eV and gamma centered Monkhorst-Pack k-grid of 12 × 10 × 8. All the simulations were carried out at experimental lattice parameters along with relaxed atomic positions using spin orbit coupling (SOC). The positions are relaxed until the Hellman-Feynman forces on each atom are less than 1×10^{-4} eV/Å. The energy surface spectrum including the momentum resolved density of states and Fermi surface properties were calculated based on the iterative Greens function method [45] after obtaining the tight-binding Hamiltonian from the maximally localized Wannier functions as implemented in the WannierTools software [46]. The defect level calculations (such as antisite and Te-vacancy) were performed for (001) surface of WTe_2 with a 4 × 3 super cell.

3 Results and discussion

3.1 Atomic and electronic structures of a cleaved WTe_2 surface

Figure 1(a) demonstrates a typical topographic image (200 nm × 200 nm) of the cleaved surface of the WTe_2 crystals, which is an atomically-flat even in a large area. The exposed surfaces of cleaved WTe_2 samples have nonuniform defect densities depending on the measured areas, so some specific locations were intentionally focused where the enough number of defects exists to investigate the interference patterns of scattering. Figure 1(b) is a STM image selectively-taken on the defect-free region (V_b = 10 mV and I_{set} = 1 nA) to demonstrate atomic corrugations of the WTe_2 surface morphology, whose atomically-ordered lattices could be also probed in the FT image of Fig. 1(b), as shown in Fig. 1(c). Figure 1(d) is the side view of the layered atomic structure of 1T'-type WTe_2, where Te atoms have two different heights due to the distortion of 1T structures in the b axis with the alternating layer stacking in the c axis. Atomic chains of the red (blue) arrow in Fig. 1(b) are composed of top (bottom) Te atoms, Te1 (Te2), along the direction. Atomic registry-dependent tunneling spectra for both Te atoms are shown in Fig. 1(e). The overall spectra of the both Te atoms represent typical semi-metallic states as expected. Even though the spectra of the occupied states (below zero gate voltage) of both Te atoms are identical, the spectra of the unoccupied states ($V_b > 0$) show a little bit difference.

3.2 Spectroscopic resonances on the Te vacancy defects

Even though the sample was cleaved *in situ* to make a bare clean surface, two types of morphologies for point defects on the exposed surface could be observed mostly. These two types of defects show the different STM images of the butterfly-like symmetry for a b-axis and the asymmetric tail feature on an a-axis with different electronic fingerprints of tunneling spectra as shown in Fig. 2. We studied in detail atomic and electronic structures of those intrinsic defects observed on the cleaved surface before analyzing the quasi-particle scattering. One typical defect image with a butterfly-like shape is shown in the zoomed-in STM image of Fig. 2(a). The position-dependent dI/dV spectra measured on the line of Fig. 2(a) were plotted in Fig. 2(b) to characterize the electronic properties of the defect. These line spectra corresponding to the LDOS show a clear double resonance peak only at the defect sites (bright spots in the figure). Away from the defect sites, the spectra are very

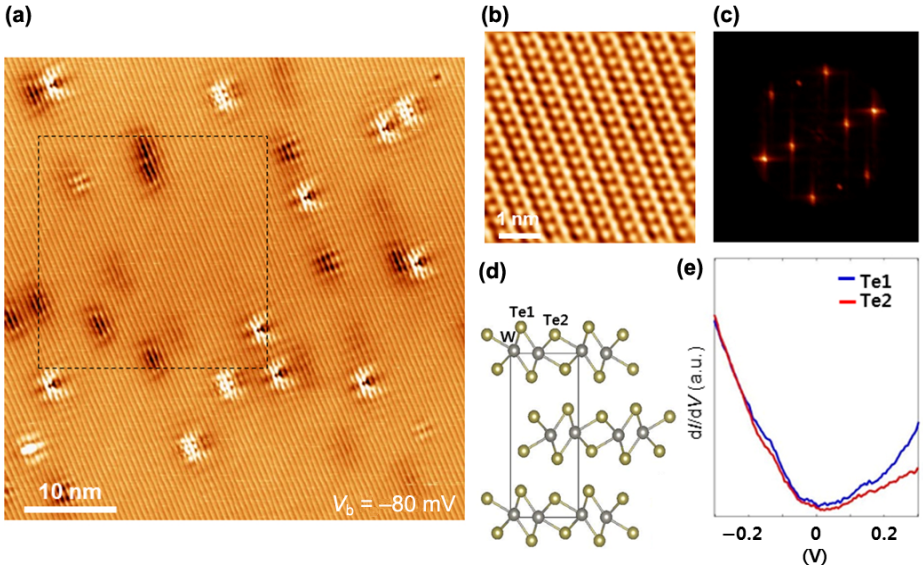

Figure 1 Atomic structure and electronic properties of WTe_2 surface. (a) Constant current STM image of the WTe_2 (001) surface (size: 200 nm × 200 nm) at V_b = 1.00 V. (b) High-resolution STM image showing atomic corrugations and (c) its FT image including symmetric lattice points. (d) Schematic of a WTe_2 crystal structure. (e) Typical dI/dV spectra measured on the surface of the defect free region.

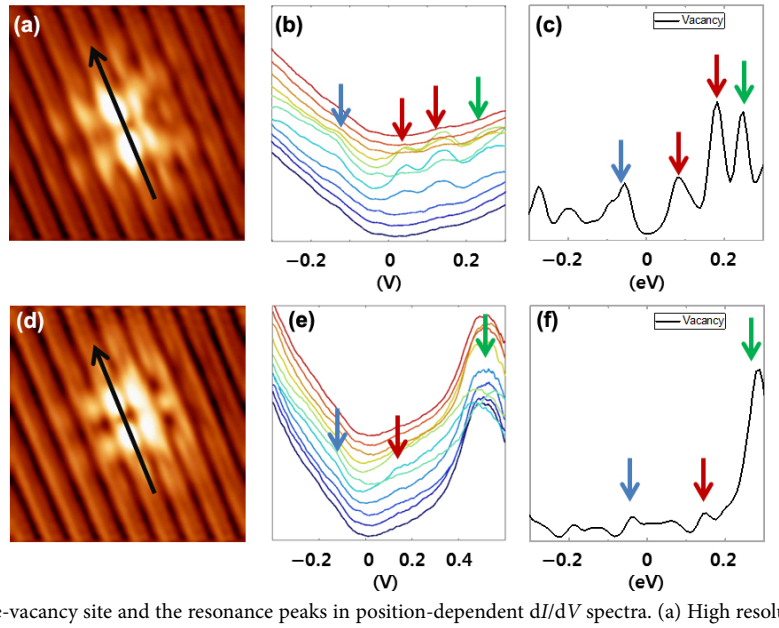

Figure 2 STM image of the Te-vacancy site and the resonance peaks in position-dependent dI/dV spectra. (a) High resolution STM image (size: 5 nm × 5 nm) of the Te2 (lower Te atom on the top surface of WTe_2) vacancy site. (b) dI/dV spectra were taken along the arrow in (a). (c) Calculated DOS based on DFT with arrows indicating the corresponding states in (b). (d) High resolution STM image (size: 5 nm × 5 nm) of the Te1 (upper Te atom on the top surface of WTe_2) vacancy site. (e) dI/dV spectra taken along the arrow in (d). (f) Calculated DOS by DFT with arrows indicating the corresponding states in (e).

similar to the LDOS of the defect-free region shown in Fig. 1(e). The resonances with double peaks are only localized to the topographically bright regions and such states are observable only within 1–2 nm from the bright regions, which indicates that additional energy states were induced by the bound states on the atomic vacancy defect site. These defect-driven spectra with the double resonances could be well confirmed by *ab initio* calculations. Figure 2(c) is a LDOS plot calculated at the Te2 (lower Te atom on the top surface of WTe_2) vacancy with color-coded arrows corresponding to those in Fig. 2(b). Two red arrows indicate the localized defect states having the double resonance, but the blue and green arrows appear as a single peak. The two resonance peaks are located at E = 46 and 136 meV above the Fermi energy. Especially, the lower energy peak occurs near the Weyl point above the Fermi energy and therefore it may be highly mixed with the surface state of the Weyl point. Figures 2(d)–2(f) represent the Te1 (upper Te atom on the top surface of WTe_2) vacancy, where the double resonance state does not appear, and the spectra look similar to the bare WTe_2 substrate only with an additional weak feature of a shoulder near 46 meV. Thus, the scattering characteristics for both vacancies look very different. Figure S1 in the Electronic Supplementary Material (ESM) shows the standing wave of the LDOS near the impurity site. The measured oscillation amplitude decays with distance from the site as $1/r^{\alpha}$ with an exponent of $\alpha \approx 1/3$, which is much slower decay than expected for impurity scattering [39, 40]. The slow decay of the amplitude is also related the strong double resonance peak near Te1 atoms.

3.3 Surface states and QPI

Based on understandings about two dominant native defects

of WTe_2 as scattering centers, energy-dependent differential conductance maps (dI/dV (eV; x, y)) have been measured to show the spatial distribution of the LDOS and to investigate QPI patterns on the cleaved surface. As a complimentary tool to ARPES, STS for spatial mapping of dI/dV spectra could be utilized to study energy-momentum dispersion relations. Although STS cannot exhibit the perpendicular component to the surface (k_z) but the lateral components (in a k_x–k_y plane) of QPI with the help of the fast Fourier transformation (FFT) of the elastic scattering patterns, STS can suggest energy-momentum dispersion for both occupied and unoccupied states as well as spatial investigations of electronic standing waves in the real space at the atomic scale.

Figure 3(a) shows the selected series of the differential conductance dI/dV maps obtained for various energies near the Fermi level on the top surface of WTe_2, where clear oscillations around the defects are shown in the energy range of 80–140 meV. The ripples of those standing waves could be observed around the defects at the surface state bands (see also Fig. S2 in the ESM for the results measured at different energies.) Figure 3(b) is the energy-dependent FT images of the corresponding dI/dV maps of Fig. 3(a) to understand the features in the reciprocal space (see also Fig. S3 in the ESM for more energy states in further detail). These energy-cut plots of QPI in panel (b) allow one to interpret the scattering channels, i.e., the arc-like features related to the surface Fermi states, in the reciprocal space. Our results show the emergence of the clear arc-like interference patterns that develop along the q_x direction at $q_x \approx 0.4$ Å^{-1}. The QPI patterns imply an anisotropic nature of the band structure, in which the spatial oscillations are strong not along the (010) direction but along the (100) direction. Figures 3(c) and 3(d) are the momentum-cut plots of QPI along the Y–Γ–Y at $X = 0$ and X–Γ–X at $Y = 0$ directions respectively in the energy range of $E - E_F = -20$ to +180 meV, i.e., the dispersion relation of the low-energy quasi-particle scattering, further highlighting the anisotropic nature of the band structure. The dispersion in q_y (Fig. 3(c)) has a node at the Γ point while there is an enhanced state at the Γ point in q_x (Fig. 3(d)). The clear and anisotropic ripples of standing waves mentioned in the Fig. 3(a), were originated from the band at the $q_y \leq 0.25$ in the energy range of 80–150 meV (a white dashed-circle in Fig. 3(c)) which was not developed along the q_x direction. These two dispersion relations can be compared with the calculated bulk band structure of WTe_2 along the same directions shown in Fig. S4 in the ESM.

3.4 Weyl-fermion-related QPI patterns

Figure 4 shows the calculated (a) spectral densities of surface states and (b) QPI patterns at various energies. Note that the projections from the bulk states have been removed in Fig. 4(a). The full spectral weights including bulk contribution were shown in Fig. S5 in the ESM. Figure 4(a) shows the surface state spectrum within the part of the first Brillouin zone. Other part can be easily obtained by symmetry. The very weak spectral densities shown in the Fig. 4(a) may be related to the bulk electronic pocket indirectly, but the structures appear due to the single particle excitation in the two dimensional scattering. Notice that the bulk spectral densities dominate over the spectral densities of surface in the most of the first Brillouin zone. In Fig. S6 in the ESM, we show the possible scattering

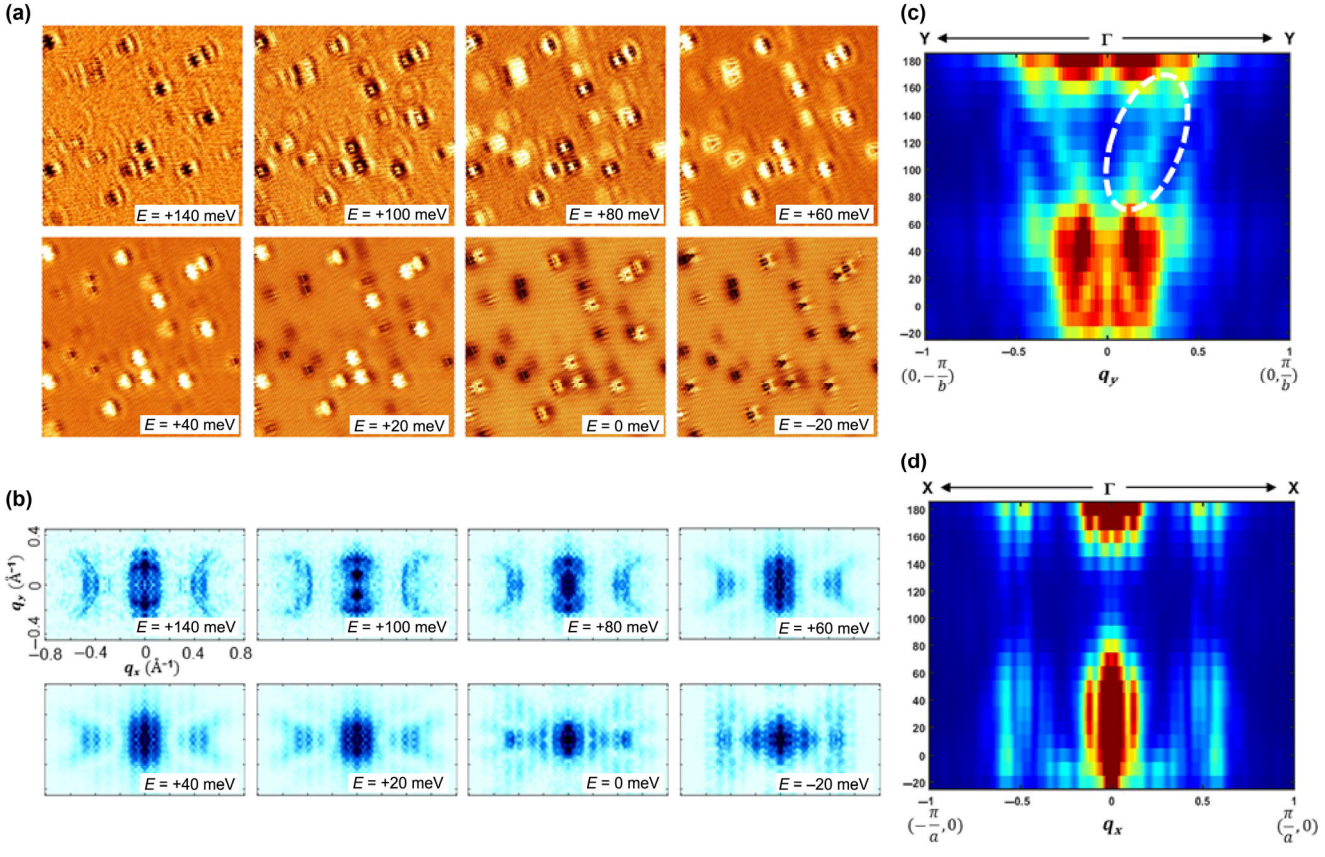

Figure 3 QPI patterns at various bias voltages from the surface of WTe_2. (a) A series of dI/dV maps measured at indicated bias voltages (size: 49 nm × 49 nm, V_b = +140, +100, +80, +60, +40, +20, 0, and −20 mV). Standing wave near the defect sites are observed in the surface state energy region. (b) Corresponding FT maps of (a). Voltage-dependent evolution of QPI patterns implies a tilted Weyl cone in the band structure. Arc-like features are observed in the FT images. (c) and (d) Energy dispersion relation, i.e., FT amplitudes of the QPI patterns, along the (c) Y–Γ–Y at $X = 0$ and (d) X–Γ–X at $Y = 0$ directions including the surface state energy region ($E = -20$ to +180 meV).

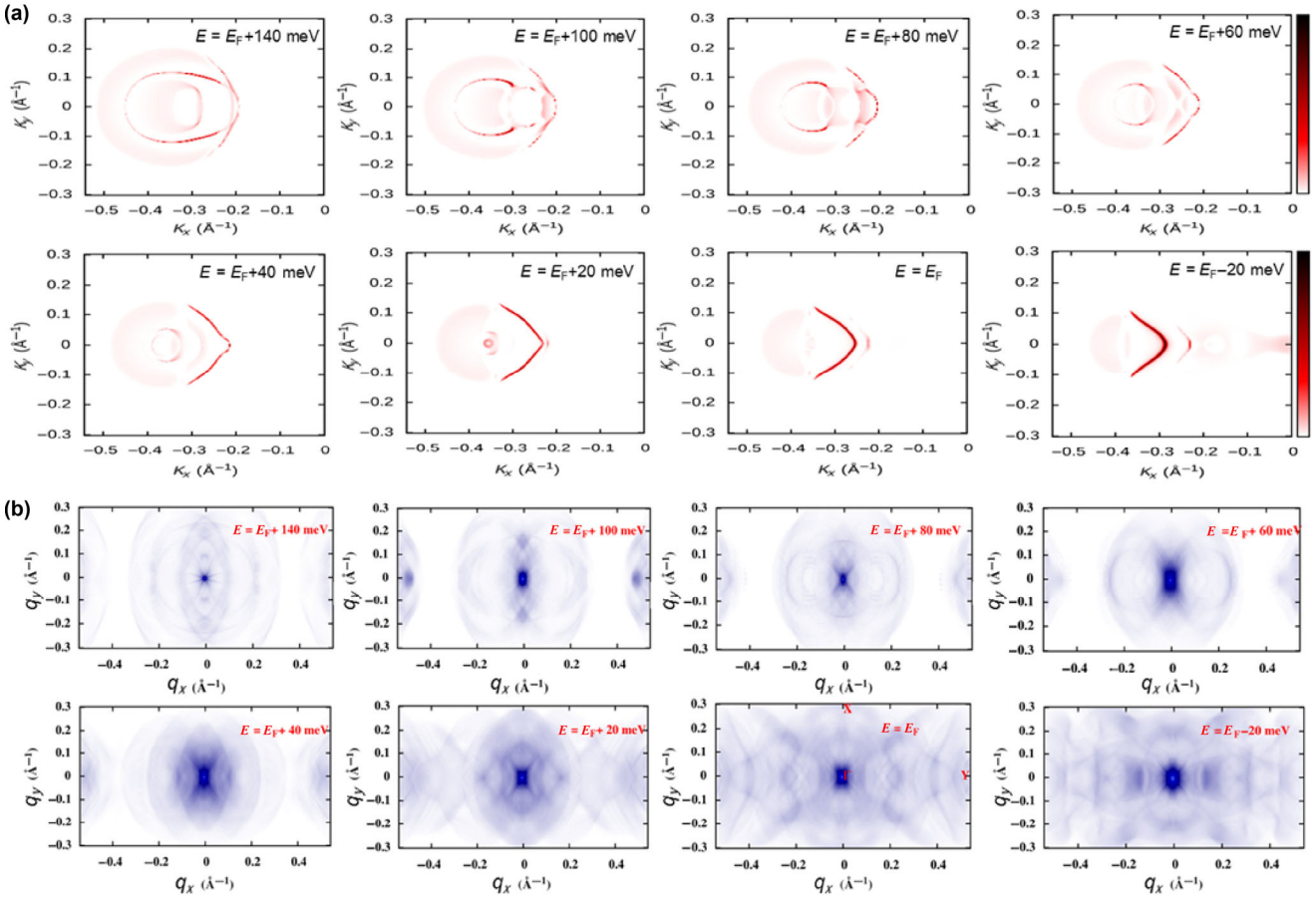

Figure 4 Simulated QPI patterns from scattering on the surface of WTe_2. (a) Calculated spectral densities of top surface states of WTe_2 and (b) the quasiparticle interference patterns for various energies. The energies shown in the figure are measured from the Fermi energy.

processes for quasiparticles and the brightness of QPI is strongly related to the available density of states for scattering. We find that the arc-like surface states are most visible up to 60 meV above the Fermi energy. As the energy increases, the arc-like surface states gradually move toward the Brillouin zone (BZ) center and completely disappear above 60 meV. This behaviour was also found in APRES experiments [29–31]. To understand more clearly the experimental features of the QPI shown in Fig. 3(b), we compare those with the calculated interference pattern. In our theoretical approach, the electronic structure of impurities and the scattering amplitude are calculated by using the T-matrix method. As shown in the experimental results in Fig. 3, an arc-like feature is clearly visible along the q_x direction, which originates from the scattering between inter-Fermi states with equal energy. The strong feature at the center of the BZ mainly originates from the scattering between intra-states. We find that, as the energy increases, the inter-states scattering features gradually move toward the center point of BZ. At energies below the Weyl points ($E < 60$ meV), trivial surface states with strong spectral densities exist. As a consequence, strong interference patterns between them appear in the experimental FT-STM images. In addition, the proximity of Weyl points in WTe_2 makes that any significant contribution of scattering from topological Fermi arcs is hardly observed in the interference patterns for WTe_2. It is also expected that since the Weyl points are very close in a reciprocal space even upon a slightly distorted structure hosting Weyl points the topological Fermi arcs connecting Weyl points may be very difficult to be observed in WTe_2.

4 Conclusion

In conclusion, we have experimentally analyzed the QPI patterns on the surface of the type-II WSM WTe_2 using STM/STS and theoretically studied those using a T-matrix approach induced by nonmagnetic impurities with the electronic properties from first-principles calculations. A clear surface state has been identified and its connection with the bulk electronic states in momentum and energy space shows a good agreement with band structure calculations. We identified a surface state emerging out of the bulk electron pocket, but it does not indicate the existence of the topologically protected Fermi arc in surface states in WTe_2. We show the interesting double resonance peaks in the LDOS appearing at localized impurities. The low-energy resonant peak occurs near the Weyl point above the Fermi energy and it may be mixed with the surface state of Weyl points, which makes it difficult to observe the topological nature of the Weyl semimetal WTe_2.

Author contributions

H. K. and E. H. designed the project. H. K. carried out the STM experiments with the help of Y. O., and I. J. and analyzed the STM data with T. J.. S. A., T. J., and E. H. performed *ab initio* calculations. S. P. and S. H. supervised the project. H. K., S. A., T. J., Y. J. S. and E. H. wrote the paper. All authors discussed the results and commented on the manuscript.

Acknowledgements

We thank K. Lee and J. Heo for useful discussions and other

colleagues at the Samsung Advanced Institute of Technology (SAIT). This work has been supported by the Global Research Laboratory Program (No. 2016K1A1A2912707), Quantum Computing Development Program (No. 2019M3E4A1080227), the Basic Science Research Program (No. 2015M3A7B4050455) and the SRC Center for Topological Matter (No. 2018R1A5A6075964) through the National Research Foundation (NRF) funded by the Ministry of Science and ICT (MSIT) in Korea. This work has been supported by Industrial Strategic Technology Development Program (No. 10085617) funded by the Ministry of Trade Industry & Energy (MOTIE) in Korea. This work has been supported by Institute for Basic Science (No. IBS-R011-D1). Supercomputing resources including technical service were supported by National Institute of Supercomputing and Network through Korea Institute of Science and Technology Information (No. KSC-2018-S1-0008).

Electronic Supplementary Material: Supplementary material (experimental analysis of the single impurity-scattering and the quasi-particle interferences is described in detail along with calculations) is available in the online version of this article at https://doi.org/10.1007/s12274-020-2892-8.

References

[1] Young, S. M.; Zaheer, S.; Teo, J. C. Y.; Kane, C. L.; Mele, E. J.; Rappe, A. M. Dirac semimetal in three dimensions. *Phys. Rev. Lett.* **2012**, *108*, 140405.

[2] Tarruell, L.; Greif, D.; Uehlinger, T.; Jotzu, G.; Esslinger, T. Creating, moving and merging Dirac points with a Fermi gas in a tunable honeycomb lattice. *Nature* **2012**, *483*, 302–305.

[3] Wang, Z. J.; Sun, Y.; Chen, X. Q.; Franchini, C.; Xu, G.; Weng, H. M.; Dai, X.; Fang, Z. Dirac semimetal and topological phase transitions in A_3Bi (A = Na, K, Rb). *Phys. Rev. B* **2012**, *85*, 195320.

[4] Singh, B.; Sharma, A.; Lin, H.; Hasan, M. Z.; Prasad, R.; Bansil, A. Topological electronic structure and Weyl semimetal in the $TlBiSe_2$ class of semiconductors. *Phys. Rev. B* **2012**, *86*, 115208.

[5] Smith, J. C.; Banerjee, S.; Pardo, V.; Pickett, W. E. Dirac point degenerate with massive bands at a topological quantum critical point. *Phys. Rev. Lett.* **2011**, *106*, 056401.

[6] Liu, C. X.; Ye, P.; Qi, X. L. Chiral gauge field and axial anomaly in a Weyl semimetal. *Phys. Rev. B* **2013**, *87*, 235306.

[7] Witczak-Krempa, W.; Kim, Y. B. Topological and magnetic phases of interacting electrons in the pyrochlore iridates. *Phys. Rev. B* **2012**, *85*, 045124.

[8] Xu, G.; Weng, H. M.; Wang, Z. J.; Dai, X.; Fang, Z. Chern semimetal and the quantized anomalous hall effect in $HgCr_2Se_4$. *Phys. Rev. Lett.* **2011**, *107*, 186806.

[9] Kobayashi, K.; Ohtsuki, T.; Imura, K. I.; Herbut, I. F. Density of states scaling at the semimetal to metal transition in three dimensional topological insulators. *Phys. Rev. Lett.* **2014**, *112*, 016402.

[10] Nandkishore, R.; Huse, D. A.; Sondhi, S. L. Rare region effects dominate weakly disordered three-dimensional dirac points. *Phys. Rev. B* **2014**, *89*, 245110.

[11] Liu, Z. K.; Zhou, B.; Zhang, Y.; Wang, Z. J.; Weng, H. M.; Prabhakaran, D.; Mo, S. K.; Shen, Z. X.; Fang, Z.; Dai, X. et al. Discovery of a three-dimensional topological dirac semimetal, Na_3Bi. *Science* **2014**, *343*, 864–867.

[12] Borisenko, S.; Gibson, Q.; Evtushinsky, D.; Zabolotnyy, V.; Büchner, B.; Cava, R. J. Experimental realization of a three-dimensional dirac semimetal. *Phys. Rev. Lett.* **2014**, *113*, 027603.

[13] Neupane, M.; Xu, S. Y.; Sankar, R.; Alidoust, N.; Bian, G.; Liu, C.; Belopolski, I.; Chang, T. R.; Jeng, H. T.; Lin, H. et al. Observation of a three-dimensional topological dirac semimetal phase in high-mobility Cd_3As_2. *Nat. Commun.* **2014**, *5*, 3786.

[14] Wan, X. G.; Turner, A. M.; Vishwanath, A.; Savrasov, S. Y. Topological semimetal and Fermi-arc surface states in the electronic structure of pyrochlore iridates. *Phys. Rev. B* **2011**, *83*, 205101.

[15] Balents, L. Weyl electrons kiss. *Physics* **2011**, *4*, 36.

[16] Burkov, A. A.; Balents, L. Weyl semimetal in a topological insulator multilayer. *Phys. Rev. Lett.* **2011**, *107*, 127205.

[17] Weng, H. M.; Fang, C.; Fang, Z.; Bernevig, B. A.; Dai, X. Weyl semimetal phase in noncentrosymmetric transition-metal monophosphides. *Phys. Rev. X* **2015**, *5*, 011029.

[18] Hosur, P.; Qi, X. L. Recent developments in transport phenomena in Weyl semimetals. *CR Phys.* **2013**, *14*, 857–870.

[19] Lv, B. Q.; Weng, H. M.; Fu, B. B.; Wang, X. P.; Miao, H.; Ma, J.; Richard, P.; Huang, X. C.; Zhao, L. X.; Chen, G. F. et al. Experimental discovery of Weyl semimetal TaAs. *Phys. Rev. X* **2015**, *5*, 031013.

[20] Xu, S. Y.; Belopolski, I.; Alidoust, N.; Neupane, M.; Bian, G.; Zhang, C.; Sankar, R.; Chang, G.; Yuan, Z.; Lee, C. C. et al. Discovery of a Weyl fermion semimetal and topological Fermi arcs. *Science* **2015**, *349*, 613–617.

[21] Yang, L. X.; Liu, Z. K.; Sun, Y.; Peng, H.; Yang, H. F.; Zhang, T.; Zhou, B.; Zhang, Y.; Guo, Y. F.; Rahn, M. et al. Weyl semimetal phase in the non-centrosymmetric compound TaAs. *Nat. Phys.* **2015**, *11*, 728–732.

[22] Batabyal, R.; Morali, N.; Avraham, N.; Sun, Y.; Schmidt, M.; Felser, C.; Stern, A.; Yan, B. H.; Beidenkopf, H. Visualizing weakly bound surface Fermi arcs and their correspondence to bulk Weyl fermions. *Sci. Adv.* **2016**, *2*, e1600709.

[23] Inoue, H.; Gyenis, A.; Wang, Z. J.; Li, J.; Oh, S. W.; Jiang, S.; Ni, N.; Bernevig, B. A.; Yazdani, A. Quasiparticle interference of the Fermi arcs and surface-bulk connectivity of a Weyl semimetal. *Science* **2016**, *351*, 1184–1187.

[24] Soluyanov, A. A.; Gresch, D.; Wang, Z. J.; Wu, Q. S.; Troyer, M.; Dai, X.; Bernevig, B. A. Type-II Weyl semimetals. *Nature*, **2015**, *527*, 495–498.

[25] Ali, M. N.; Xiong, J.; Flynn, S.; Tao, J.; Gibson, Q. D.; Schoop, L. M.; Liang, T.; Haldolaarachchige, N.; Hirschberger, M.; Ong, N. P. et al. Large, non-saturating magnetoresistance in WTe_2. *Nature* **2014**, *514*, 205–208.

[26] Kang, D. F.; Zhou, Y. Z.; Yi, W.; Yang, C. L.; Guo, J.; Shi, Y. G.; Zhang, S.; Wang, Z.; Zhang, C.; Jiang, S. et al. Superconductivity emerging from a suppressed large magnetoresistant state in tungsten ditelluride. *Nat. Commun.* **2015**, *6*, 7804.

[27] Pan, X. C.; Chen, X. L.; Liu, H. M.; Feng, Y. Q.; Wei, Z. X.; Zhou, Y. H.; Chi, Z. H.; Pi, L.; Yen, F.; Song, F. Q. et al. Pressure-driven dome-shaped superconductivity and electronic structural evolution in tungsten ditelluride. *Nat. Commun.* **2015**, *6*, 7805.

[28] Wu, Y.; Mou, D. X.; Jo, N. H.; Sun, K. W.; Huang, L. N.; Bud'ko, S. L.; Canfield, P. C.; Kaminski, A. Observation of Fermi arcs in the type-II Weyl semimetal candidate WTe_2. *Phys. Rev. B* **2016**, *94*, 121113.

[29] Bruno, F. Y.; Tamai, A.; Wu, Q. S.; Cucchi, I.; Barreteau, C.; de la Torre, A.; McKeown Walker, S.; Riccò, S.; Wang, Z.; Kim, T. K. et al. Observation of large topologically trivial Fermi arcs in the candidate type-II Weyl semimetal WTe_2. *Phys. Rev. B* **2016**, *94*, 121112.

[30] Sánchez-Barriga, J.; Vergniory, M. G.; Evtushinsky, D.; Aguilera, I.; Varykhalov, A.; Blügel, S.; Rader, O. Surface Fermi arc connectivity in the type-II Weyl semimetal candidate WTe_2. *Phys. Rev. B* **2016**, *94*, 161401.

[31] Feng, B. J.; Chan, Y. H.; Feng, Y.; Liu, R. Y.; Chou, M. Y.; Kuroda, K.; Yaji, K.; Harasawa, A.; Moras, P.; Barinov, A. et al. Spin texture in type-II Weyl semimetal WTe_2. *Phys. Rev. B* **2016**, *94*, 195134.

[32] Wang, C. L.; Zhang, Y.; Huang, J. W.; Nie, S. M.; Liu, G. D.; Liang, A. J.; Zhang, Y. X.; Shen, B.; Liu, J.; Hu, C. et al. Observation of Fermi arc and its connection with bulk states in the candidate type-II Weyl semimetal WTe_2. *Phys. Rev. B* **2016**, *94*, 241119.

[33] Sprunger, P. T.; Petersen, L.; Plummer, E. W.; Lægsgaard, E.; Besenbacher, F. Giant Friedel oscillations on the beryllium(0001) surface. *Science* **1997**, *275*, 1764–1767.

[34] Seo, J.; Roushan, P.; Beidenkopf, H.; Hor, Y. S.; Cava, R. J.; Yazdani, A. Transmission of topological surface states through surface barriers. *Nature* **2010**, *466*, 343–346.

[35] Okada, Y.; Dhital, C.; Zhou, W. W.; Huemiller, E. D.; Lin, H.; Basak, S.; Bansil, A.; Huang, Y. B.; Ding, H.; Wang, Z. et al. Direct

observation of broken time-reversal symmetry on the surface of a magnetically doped topological insulator. *Phys. Rev. Lett.* **2011**, *106*, 206805.

[36] Simon, L.; Bena, C.; Vonau, F.; Cranney, M.; Aubel, D. Fourier-transform scanning tunnelling spectroscopy: The possibility to obtain constant-energy maps and band dispersion using a local measurement. *J. Phys. D: Appl. Phys.* **2011**, *44*, 464010.

[37] Kresse, G.; Furthmüller, J. Efficiency of *ab-initio* total energy calculations for metals and semiconductors using a plane-wave basis set. *Comput. Mater. Sci.* **1996**, *6*, 15–50.

[38] Kresse, G.; Furthmüller, J. Efficient iterative schemes for *ab initio* total-energy calculations using a plane-wave basis set. *Phys. Rev. B* **1996**, *54*, 11169–11186.

[39] Chen, L.; Cheng, P.; Wu, K. H. Quasiparticle interference in unconventional 2D systems. *J. Phys.: Condens. Matter* **2017**, *29*, 103001.

[40] Wang, J.; Li, W.; Cheng, P.; Song, C. L.; Zhang, T.; Deng, P.; Chen, X.; Ma, X. C.; He, K.; Jia, J. F. et al. Power-Law decay of standing waves on the surface of topological insulators. *Phys. Rev. B* **2011**, *84*, 235447.

[41] Ceperley, D. M.; Alder, B. J. Ground state of the electron gas by a stochastic method. *Phys. Rev. Lett.* **1980**, *45*, 566–569.

[42] Perdew, J. P.; Zunger, A. Self-interaction correction to density-functional approximations for many-electron systems. *Phys. Rev. B* **1981**, *23*, 5048–5079.

[43] Blöchl, P. E. Projector augmented-wave method. *Phys. Rev. B* **1994**, *50*, 17953–17979.

[44] Kresse, G.; Hafner, J. *Ab initio* molecular dynamics for open-shell transition metals. *Phys. Rev. B* **1993**, *48*, 13115–13118.

[45] Sancho, M. P. L.; Sancho, J. M. L.; Sancho, J. M. L.; Rubio, J. Highly convergent schemes for the calculation of bulk and surface green functions. *J. Phys. F: Met. Phys.* **1985**, *15*, 851–858.

[46] Wu, Q. S.; Zhang, S. N.; Song, H. F.; Troyer, M.; Soluyanov, A. A. WannierTools: An open-source software package for novel topological materials. *Comput. Phys. Commun.* **2018**, *224*, 405–416.